Acta Oceanol. Sin., 2020, Vol. 39, No. 11, P. 1–12
https://doi.org/10.1007/s13131-020-1671-4
http://www.hyxb.org.cn
E-mail: hyxbe@263.net

Dynamical analysis of submesoscale fronts associated with wind-forced offshore jet in the western South China Sea

Xiaolong Huang[1, 2], Zhiyou Jing[1, 3, 4]*, Ruixi Zheng[1, 2], Haijin Cao[5]

[1] State Key Laboratory of Tropical Oceanography, South China Sea Institute of Oceanology, Chinese Academy of Sciences, Guangzhou 510301, China

[2] University of Chinese Academy of Sciences, Beijing 100049, China

[3] Southern Marine Science and Engineering Guangdong Laboratory (Guangzhou), Guangzhou 511458, China

[4] Innovation Academy of South China Sea Ecology and Environmental Engineering, Chinese Academy of Sciences, Guangzhou 510301, China

[5] College of Oceanography, Hohai University, Nanjing 210024, China

Received 13 April 2020; accepted 8 July 2020

Abstract

This study investigates the submesoscale fronts and their dynamic effects on the mean flow due to frontal instabilities in the wind-driven summer offshore jet of the western South China Sea (WSCS), using satellite observations, a 500 m-resolution numerical simulation, and diagnostic analysis. Both satellite measurements and simulation results show that the submesoscale fronts occupying a typical lateral scale of O(~10) km are characterized with one order of Rossby (*Ro*) and Richardson (*Ri*) numbers in the WSCS. This result implies that both geostrophic and ageostrophic motions feature in these submesoscale fronts. The diagnostic results indicate that a net cross-frontal Ekman transport driven by down-front wind forcing effectively advects cold water over warm water. By this way, the weakened local stratification and strong lateral buoyancy gradients are conducive to a negative Ertel potential vorticity (PV) and triggering frontal symmetric instability (SI) at the submesoscale density front. The cross-front ageostrophic secondary circulation caused by frontal instabilities is found to drive an enhanced vertical velocity reaching O(100) m/d. Additionally, the estimate of the down-front wind forcing the Ekman buoyancy flux (EBF) is found to be scaled with the geostrophic shear production (GSP) and buoyancy flux (BFLUX), which are the two primary energy sources for submesoscale turbulence. The large values of GSP and BFLUX at the fronts suggest an efficient downscale energy transfer from larger-scale geostrophic flows to the submesoscale turbulence owing to down-front wind forcing and frontal instabilities. In this content, submesoscale fronts and their instabilities substantially enhance the local vertical exchanges and geostrophic energy cascade towards smaller-scale. These active submesoscale processes associated density fronts and filaments likely provide new physical interpretations for the filamentary high chlorophyll concentration and frontal downscale energy transfer in the WSCS.

Key words: submesoscale fronts, enhanced vertical velocity, energy transfer, offshore jet, western South China Sea

Citation: Huang Xiaolong, Jing Zhiyou, Zheng Ruixi, Cao Haijin. 2020. Dynamical analysis of submesoscale fronts associated with wind-forced offshore jet in the western South China Sea. Acta Oceanologica Sinica, 39(11): 1–12, doi: 10.1007/s13131-020-1671-4

1 Introduction

Upper ocean circulation, significantly influenced by atmospheric forcing consists of motions of a broad range of scales (Wunsch and Ferrari, 2004; Thomas and Taylor, 2010). The submesoscale fronts, which constitute an asymmetrical atmospheric forcing (e.g., down-front wind forcing and surface cooling), can be frequently detected from high-resolution satellite observations (Zheng et al., 2008; Liu et al., 2015; Liu and Levine, 2016). These elongated fronts are dynamically characterized by O(1) Rossby number (*Ro*) and Richardson number (*Ri*). In addition, they possess a typical lateral scale of O(1–10) km and a time scale of O(hour–day) (Thomas et al., 2008). For such space and time scales, the assumption of geostrophy is no longer valid (Gula et al., 2014; McWilliams, 2017, 2019). Thus, dynamic processes involved in submesoscale fronts or filaments include both geostrophic and ageostrophic motions. Furthermore, the ageostrophic processes associated with the submesoscale instabilities can produce significant divergent flows and stir up a large vertical velocity, thus substantially contributing to the enhanced vertical fluxes of heat, buoyancy, nutrient, and momentum in the upper oceans (Mahadevan and Tandon, 2006; Su et al., 2018; Zhang et al., 2019). The frontal instabilities at submesoscales have been detected to be able to extract kinetic energy (KE) from the larger-scale geostrophic flows, and cascade energy towards

Foundation item: This work is supported by the Chinese Academy of Sciences under contract Nos ZDBS-LY-DQC011, ZDRW-XH-2019-2 and ISEE2018PY05; the Southern Marine Science and Engineering Guangdong Laboratory (Guangzhou) under contract No. GML2019ZD0303; the National Natural Science Foundation of China under contract Nos 41776040 and 92058201; the Pilot National Laboratory for Marine Science and Technology (Qingdao) under contract No. OCFL-201804; the State Key Laboratory of Tropical Oceanography under contract No. LTO1907; the Guangzhou Science and Technology Project under contract No. 201904010420.
*Corresponding author, E-mail: jingzhiyou@scsio.ac.cn

smaller scales (Mcwilliams et al., 2001; D'Asaro et al., 2011). These phenomena are widely viewed in the ocean and are interpreted as a bridge between the mesoscale and small-scale motions (Capet et al., 2008; McWilliams, 2016).

The upper basin-scale circulation of the South China Sea (SCS) is mostly dominated by the east Asian monsoon system with a distinct seasonal cycle (Wyrtki, 1961). A three-dimensional ocean model with a high frequency atmospheric force is utilized to study the seasonal characteristics of flow and its associated dynamic analysis in SCS (Gan et al., 2006). Abundant mesoscale eddies are observed to be embedded in the seasonal circulation (Chu et al., 1998; Chen et al., 2011; Zhang et al., 2016; Xie and Zheng, 2017; Xie et al., 2018). The statistical properties of the mesoscale eddies and their spatio-temporal variability are widely studied using satellite altimeter data in the SCS (Wang et al., 2003; Chen et al., 2011; Zheng et al., 2017; He et al., 2018). A weeklong field campaign in the western South China Sea (WSCS) has revealed a three-dimensional structure and physical properties of a typical cold eddy, as well as its underlying forcing mechanism for the formation of the cyclonic cold eddy (Hu et al., 2011). These active eddies in the SCS are found to be effecting the biogeochemical cycles through upwelling and downwelling (Xiu and Chai, 2011), the dissipation of mesoscale eddies (Yang et al., 2019) and contributing energy transfer and vertical exchanges via multi-scale interactions (Chen et al., 2012). The southeast of Vietnam is an eddy active zone of the SCS with a high eddy kinetic energy (EKE) estimated from altimeter measurements (Fig. 1a). The unique orographic wind jet could be one of main reasons for the strong mesoscale variability in the WSCS (Wang et al., 2008).

As shown in Fig. 1b, the SST and the surface current during the summer suggest that the summer offshore jet with surface cooling is a common phenomenon in the WSCS because of the southwest wind forcing (Kuo et al., 2000; Xie et al., 2003). The offshore jet and its associated flow variation are investigated by a high-resolution region ocean model and it is found that the coastal currents induced by the wind forcing and shelf topography contributed to the coastal jet separation (Gan and Qu, 2008). At the same time, the jet separation is also generated by a combination of wind stress, river discharge, and vorticity transport, which are originated from the coast off Vietnam and located around 12°N, between 110° and 113°E (Wang et al., 2006; Li et al., 2014). Owing to its underlying importance in the multi-scale interactions, enhanced air-sea communication, and regional ecosystem, the far-extended offshore jet has been widely investigated in the past decade, especially on its intra-seasonal, seasonal, inter-annual, and inter-decadal variations (Fang et al., 2002; Xie et al., 2007; Wang et al., 2010; Chen and Wang, 2014; Li et al., 2014). In summer, the upwelled cold water is advected offshore, as detected from the satellite images in the filament-shaped upwelled frontal zones (Metzger, 2003; Liu et al., 2015).

The SCS is a region with active submesoscale processes (Zheng et al., 2020). In the WSCS, submesoscale structures with a length scale of 10 km are frequently detected in high-resolution ocean color images, which are generated on the frontal system of the cold jet (Liu et al., 2015). An active submesoscale vortex in the WSCS is also examined using ocean color observations and a high-resolution simulation (Yu et al., 2018). Although these submesoscale phenomena are viewed by high-resolution satellite observations, the dynamic characteristics of the submesoscale processes on the frontal system have not been well understood so far. In this study, we examine the dynamic features of the submesoscale density fronts and their potential effects on the vertical communication and energy cascade in the offshore jet of the WSCS, using a fine-resolution simulation and satellite measurements. The remainder of this paper is organized as follows. Section 2 describes the satellite data, fine-resolution simulations, and related dynamic parameters. Section 3 discusses the features of the submesoscale fronts under the influence of down-front wind forcing. Section 4 analyzes the forward energy transfer through submesoscale instabilities. Finally, Section 5 summarizes the results from this study.

2 Data and methods

2.1 *Satellite remote sensing data*

The primary satellite datasets used in this study include high-resolution SST data, sea level anomaly (SLA) data, sea surface wind field data, and MEdium Resolution Imaging Spectrometer (MERIS) chlorophyll *a* data. The high resolution SST data are provided by the U.K. Meteorological Office and comprise 6 km×6 km daily products, distributed by the Group for High Resolution Sea Surface Temperature (GHRSST) project (http://data.nodc.

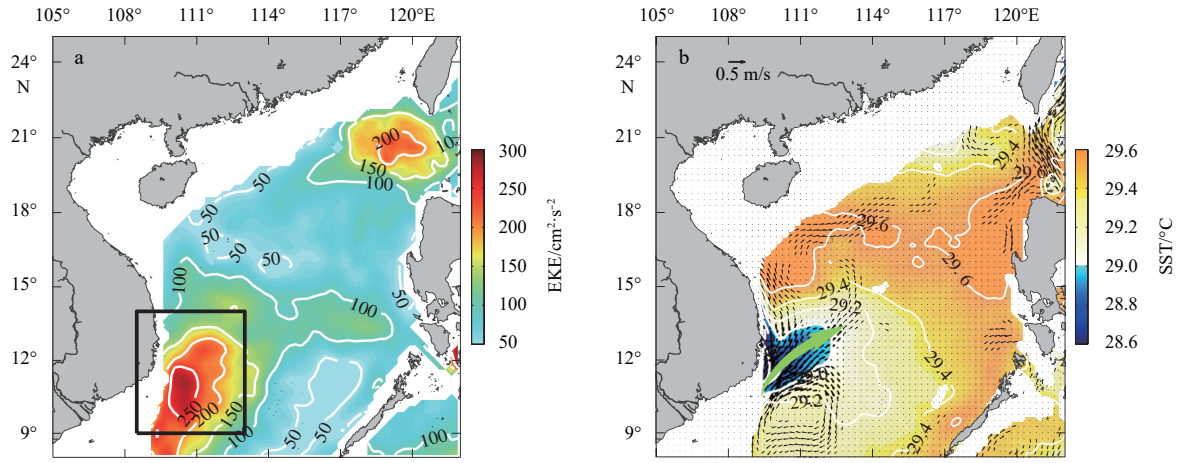

Fig. 1. Climatological EKE and sea surface temperature (SST) in the SCS. a. EKE based on 30–90 d band-pass filtered satellite altimeter SLA data from October 1992 to August 2016; and b. climatological SST distribution in the SCS during summer. The black box in a denotes the WSCS (9°–14°N, 108.5°–113°E); the black vectors and the green arrow marks in b indicate the geostrophic current (> 0.1 m/s) and the offshore jet, respectively.

noaa.gov/ghrsst/L4/GLOB/UKMO/OSTIA/), and merged with *in situ*, microwave, and infrared satellite data (Donlon et al., 2012). The daily SLA datasets are distributed by the French archiving, validation and interpretation of satellite oceanographic (AVSIO) setup and range from October 1992 to August 2016, with a spatial resolution of 0.25°×0.25°. This gridded SLA product is merged with TOPEX/Poseidon (T/P), Jason, ERS-1, ERS-2, and ENVISAT (ftp://ftp.aviso.oceanobs.com/global/). The daily surface winds are obtained from the NOAA National Climatic Data Center (NCDC) (ftp://eclipse.ncdc.noaa.gov/pub/seawinds/) at a 0.25° resolution (Zhang et al., 2006). The sea surface chlorophyll *a* concentration data are derived from the MERIS Level 2 Full Resolution Full Swath (FRS) dataset from May 17, 2002 to April 8, 2012 (ftp://merisfrs-ftp-ds.eo.esa.int). This dataset provides observations at high temporal, spatial (~300 m), and spectral resolution, and with a higher sensitivity than is provided by other satellite sensors, thus allowing us have new insights into the fine structure of the surface fronts and filaments.

A fine-resolution nested Regional Oceanic Modeling System (ROMS) (Shchepetkin and McWilliams, 2005) is used to investigate the submesoscale processes in this study. The boundary and initial conditions of the model are derived from the monthly datasets of simple ocean data assimilation (SODA) (Carton and Giese, 2008). The simulations are forced by wind stress and atmospheric forcing. The wind forcing is from a daily mean climatology Quick Scatterometer (QuikSCAT) dataset (Risien and Chelton, 2008). The atmospheric forcing related to heat and freshwater fluxes are derived from the monthly climatology of the international Comprehensive Ocean-Atmosphere Data Set (ICOADS) (Woodruff et al., 2011). The bathymetry data for all the domains are obtained from the British Oceanographic Date Centre (BODC) (https://www.bodc.ac.uk/data/) based on the 30 arc-s dataset of General Bathymetric Chart of the Oceans (GEBCO).

2.2 *Model setup*

The online nesting of the ROMS utilizes an approach of successive horizontal grid refinements from a parent grid (ROMS0) to two nested child grids (ROMS1 and ROMS2) (Penven et al., 2006; Gula et al., 2015). The model has 60 levels in terrain-following vertical *S*-coordinates with concentrated levels in the boundary layers (Lemarié et al., 2012). The vertical subgrid mixing of tracers and momentum is based on the K-profile parameterization (KPP) (Large et al., 1994).

The ROMS0 with a grid resolution of approximately 7.5 km covers the entire western Pacific, which reaches an equilibrium state after a 20-year spin up, and then runs an additional two years to provide daily boundary information for the SCS (ROMS1, which has a grid resolution of approximately 1.5 km) and the WSCS (ROMS2, which has an approximate grid solution of 500 m) (Fig. 2). All of these nested models have a daily mean output in the 21st model year. In this study, the high-resolution results of ROMS2 are used to analyze the submesoscale fronts on the eastward jet of the WSCS.

2.3 *Diagnostic calculations of the submesoscale front*

As an important dynamic tracer, the potential vorticity (PV) significantly affects the hydrostatic and geostrophic balance, and reflects the stability of the oceanic flow (Hoskins, 1974; Thomas, 2005; Thomas et al., 2013). Different types of instabilities develop when the Ertel PV takes the opposite sign of the Coriolis parameter *f*. The Ertel PV, denoted by *q*, is given by (Hoskins, 1974):

$$q = \omega_a \cdot \nabla b = \mathrm{EPV_v} + \mathrm{EPV_h} = (f+\zeta)N^2 + \omega_h \cdot \nabla_h b, \quad (1)$$

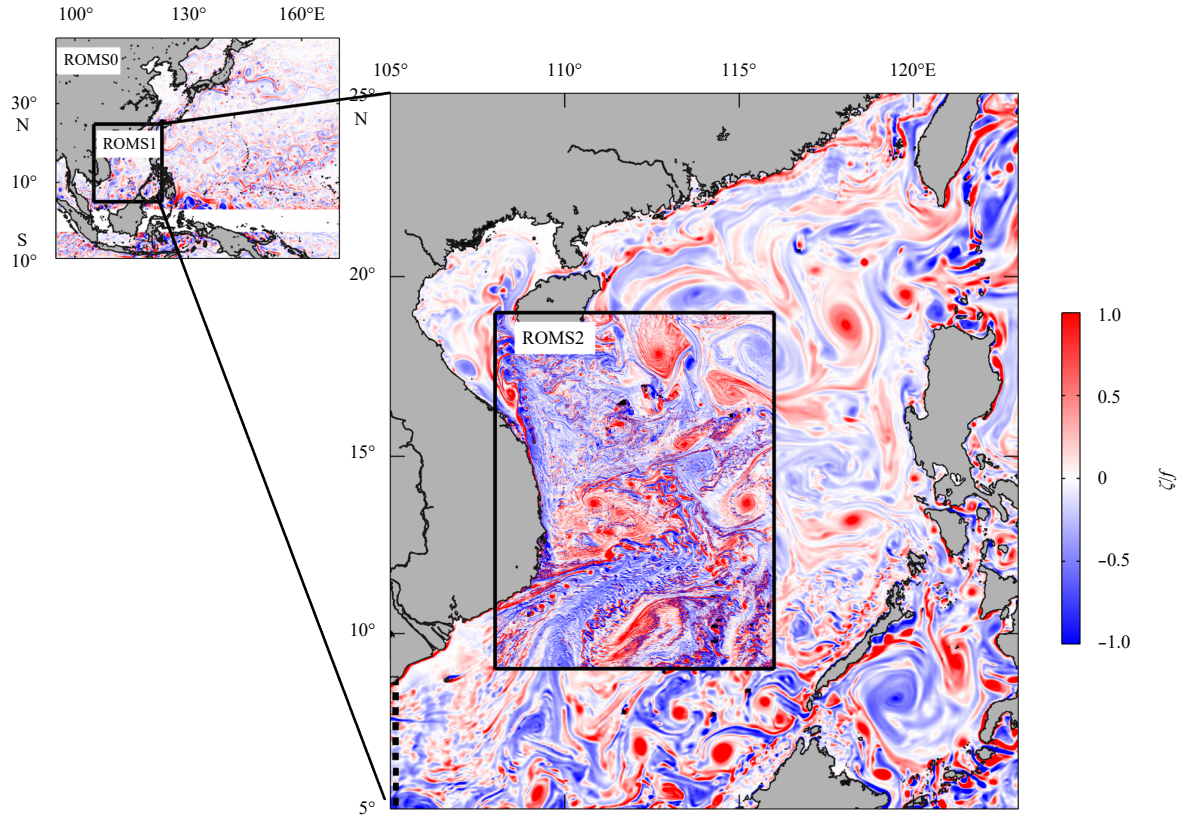

Fig. 2. Maps of Rossby number ($Ro = \zeta/f$) from ROMS0, ROMS1, and ROMS2 (black rectangle) simulation in the WSCS.

where $\omega_a = f\boldsymbol{k} + \nabla \times \boldsymbol{u}$ is the absolute vorticity, in which $\boldsymbol{k}$ is local vertical unit vector; $b = -g\rho/\rho_0$ is the buoyancy (g is the gravitational acceleration, ρ is the potential density, and ρ_0 is the reference density); and ∇b refers to the buoyancy gradient. $(f+\zeta)$ and ω_h are the vertical and horizontal components of ω_a, respectively. $\zeta = \partial v/\partial x - \partial u/\partial y$ is the relative vorticity; and $N^2 = -\frac{g}{\rho_0}\frac{\partial \rho}{\partial z}$ is the buoyancy frequency. The last two terms of Eq. (1) are the horizontal component (Ertel PV_h, i.e., EPV_h) and vertical component (Ertel PV_v, i.e., EPV_v) of the Ertel PV, respectively.

For a geostrophic flow, the Ertel PV_h using the thermal wind relation can be approximately written as:

$$\text{Ertel PV}_\text{h} \approx -f\left|\frac{\partial \boldsymbol{u}_g}{\partial z}\right|^2 = -\frac{|\nabla_\text{h} b|^2}{f}. \tag{2}$$

The Ertel PV_h is negative definite and plays a role in reducing the PV in the northern hemisphere. Moreover, the last term of Eq. (2) illuminates that the Ertel PV_h is contributed by a sharp lateral buoyancy gradient forced by the geostrophic flow vertical shear (Boccaletti et al., 2007). The strength of the lateral buoyancy gradient can be expressed by the frontal sharpness (Gula et al., 2016),

$$M^4 = |\nabla_\text{h} b|^2/2. \tag{3}$$

The wind-work is conducive to changing the buoyancy field in the upper ocean. The effect of the Ekman transport advecting buoyancy can be expressed in terms of the Ekman buoyancy flux (EBF) (Thomas, 2005):

$$\text{EBF} = M_\text{e} \cdot \nabla_\text{h} b|_{z=0}, \quad M_\text{e} = (\tau_y/f\rho_0, -\tau_x/f\rho_0), \tag{4}$$

where M_e is the Ekman transport and (τ_x, τ_y) is the wind stress vector.

A negative PV is a key parameter to diagnose the frontal instabilities (e.g., symmetric instability (SI)). SI is a type of shear instability at submesoscale, which can draw KE from the background geostrophic flow (Taylor and Ferrari, 2009; Thomas, 2012). The rate at which the shear instabilities extract geostrophic KE can be represented by the geostrophic shear production (GSP) (Thomas and Taylor, 2010):

$$\text{GSP} = -\overline{u'w'}\frac{\partial \bar{u}_g}{\partial z}, \tag{5}$$

where the overbars and primes denote spatial averaged and perturbations from the average, respectively; u_g refers to the geostrophic velocity; and w is the vertical velocity from the simulations. Similarly, the buoyancy flux (BFLUX) can be used to estimate the rate of releasing the available potential energy (APE) stored in the front (Fox-Kemper et al., 2008):

$$\text{BFLUX} = \overline{w'b'}, \tag{6}$$

where b' denotes the abnormal buoyancy after subtracting the spatial average.

3 Fine structure and dynamic features of the density front

In Fig. 3a, a conspicuous feature is that the upwelled cold water (<27.5°C) is pumped from the subsurface water in the coastal region and is advected to the east. The offshore cold jet from the coast also causes an offshore transport of the coastal upwelled nutrition (>1 mg/m^3) (the tongue-shaped ocean color image with a high chlorophyll *a* concentration on a lateral scale of approximately 30 km in Fig. 3b). Furthermore, active fine structures can be observed in the periphery of high chlorophyll *a*, which is also an active thermal front zone. These structures are roughly within the submesoscale range.

Although snapshots of ocean color image provide observational evidence for the submesoscale structures near the eastward jet (Liu et al., 2015), they cannot support a dynamic interpretation for the submesoscale motions, as they are fast evolving. To further analyze submesoscale dynamical processes associated with wind forcing in the WSCS upwelling zone. A representative and clean filamentary case with strong lateral buoyancy gradients is selected from the ROMS2 results. Figure 4 shows their snapshots of spatial characteristics and zoomed structures on August 4. These simulation results have been evaluated against the limited historical observations and reanalysis data. The comparisons to measurements show that the simulations are reliable to characterize the upwelling and front conditions.

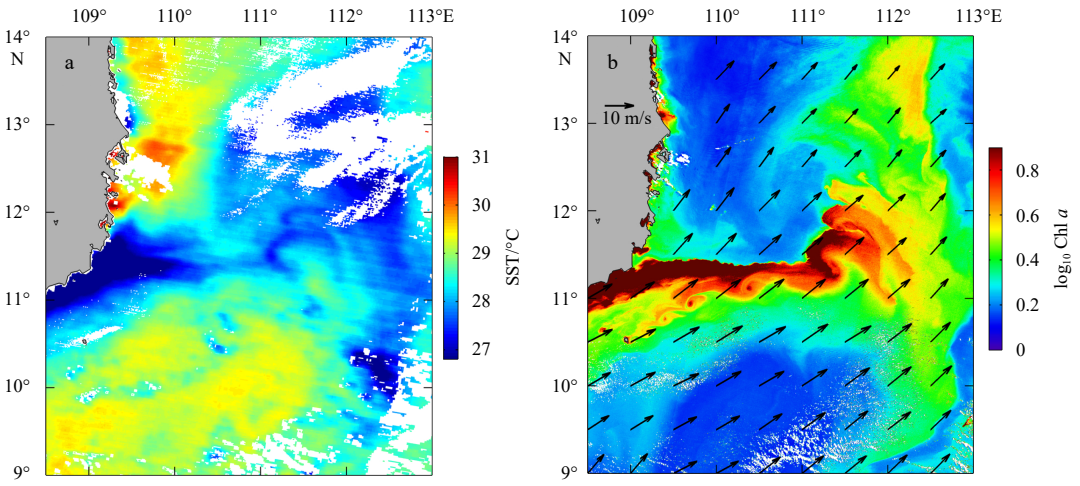

Fig. 3. Spatial distribution of SST of the Moderate Resolution Imaging Spectroradiometer (MODIS) in the WSCS (black box shown in Fig. 1) (a); and maps of chlorophyll *a* concentration (mg/m^3, shading) base 10 log and wind vectors on July 26, 2009 (b).

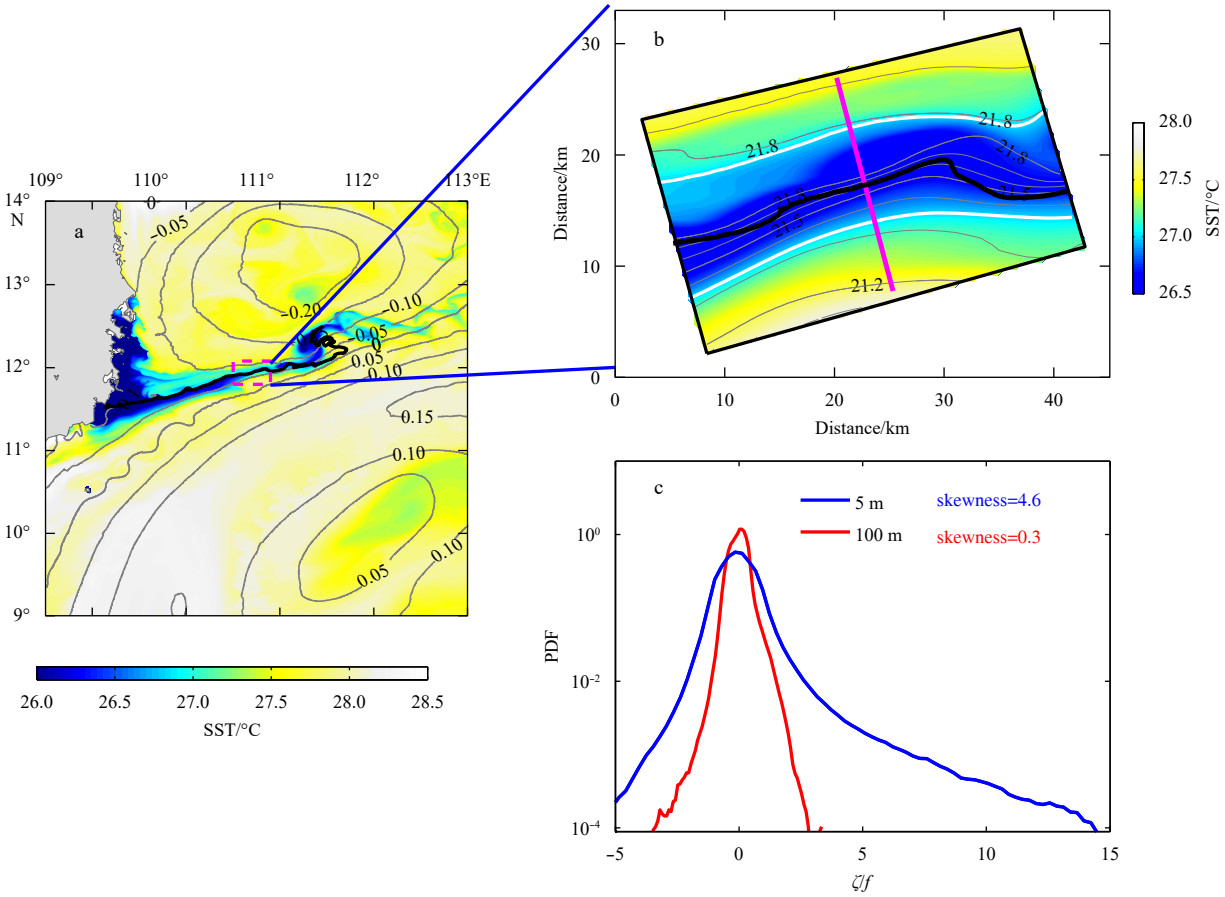

Fig. 4. Snapshot of the SST (shading) and eastward jet (bold black line) in the WSCS from ROMS2 simulation at 13:00 on August 4, 21 model years (a) (the gray contours denote the SLA, unit: m); the SST zoomed into the rectangles of Fig. 4a (b); and probability density function (PDF) of *Ro* within a dashed rectangle in Fig. 4b (c), refers to the frontal zone of jet (11.8°–12.1°N, 110.57°–111°E) at depths of 5 m and 100 m, respectively.

The diagnostic parameters are estimated for the sub-region (Fig. 4b, 11.8°–12.1°N, 110.57°–111°E) as explained below to show the fine dynamic features of the submesoscale fronts in the summer offshore cold jet. Here we define the zero vorticity contour as the jet axis according to Chen and Wang (2014). In this frontal zone, the probability density function (PDF) of $Ro(\zeta/f)$ tends to be asymmetric with a positive skewness at the surface layer (5 m) compared to that at 100 m (Fig. 4c). It exhibits a feature that $O(1)$ *Ro* widely exists in the upper ocean of the frontal zone of jet. This implies a departure from the balanced geostrophic prediction (Dong and Zhong, 2018). As a result, this frontal zone with enhanced lateral buoyance gradients has a favorable situation for the occurrence of submesoscale processes. Owing to the presence of the wind forcing and offshore cold jet, the enhanced frontal sharpness normalized by f^3 can be clearly detected along the elongated front (Fig. 5a). The frontal sharpness has a peak

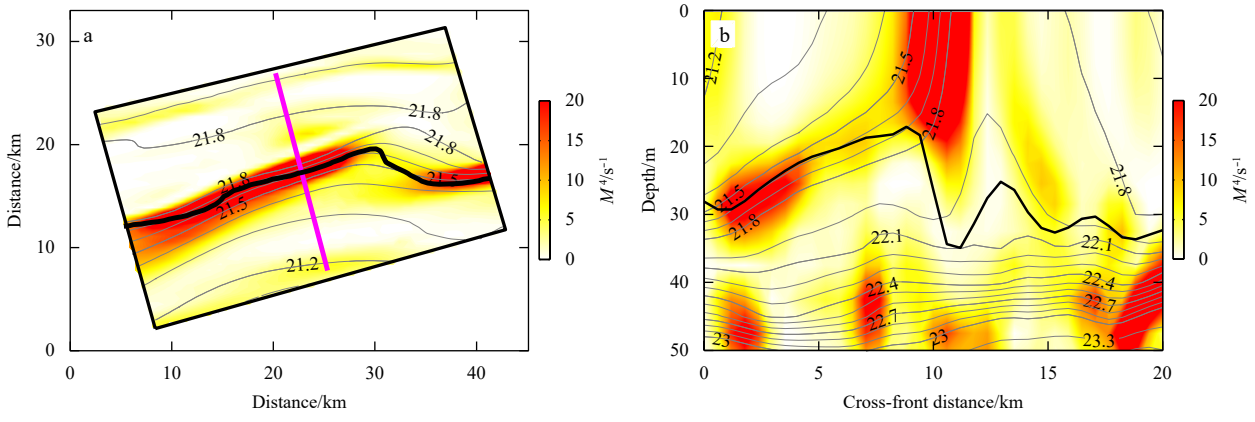

Fig. 5. Frontal sharpness (M^4, shading) normalized by f^3: horizontal distribution of the frontal sharpness (a); vertical profiles of the frontal sharpness (b). The MLD is shown as black lines. The gray contours refer to isopycnals with a spacing of 0.1 kg/m^3.

within a width of approximately 5 km between the outcropping isopycnals of 21.4 and 21.8 near the surface eastward jet. The across-front section (magenta solid line in Fig. 5a) is mapped to show its vertical profile (Fig. 5b). The submesoscale density front is mostly active in the upper mixed layer with a strong frontal sharpness. Furthermore, some scattered strong frontal sharpness can be seen at the base of the mixed layer (MLD) owing to the mixed layer instability.

Figure 6 presents the divergence ($\delta = u_x + v_y$) and vertical velocity to illustrate the ageostrophic effect at the frontal zone. The instantaneous vertical velocity is characterized with a positive-negative pattern, similar to the horizontal divergence. It means that the convergence appears in the frontal jet, where the downwelling can reach 100 m/d and is one order of magnitude larger than the typical mesoscale effects (Mahadevan and Tandon, 2006), which substantially enhances the local vertical exchanges.

The temperature and along-front perturbation velocity in the vertical section show a typical ageostrophic secondary circulation across the submesoscale front (Fig. 7). The secondary circulations have a double-cell structure with dowelling on the dense side of the front and upwelling on the light side away from the front, which acts to restratify the MLD, and release the frontal APE. As a result, on the cold side of the recirculation cell, the maximum downwelling can reach approximately 100 m/d (Fig. 7b). The intensified ageostrophic vertical velocities can penetrate into the ocean interior, and substantially enhance the vertical communication of momentum and tracers between the surface and the oceanic interior.

Some theoretical studies have found that the strong secondary circulation in the submesoscale front is closely related to the frontal instabilities (Mahadevan and Tandon, 2006; McWilliams, 2016). The negative PV in the flow is a sufficient criterion for the SI (Thomas et al., 2013). In a typical front considered in this study, the Ertel PV_h is non-negligible in comparison to the Ertel PV_v because of the strong lateral buoyancy gradient, enhanced vertical shear, and decreased local stratification in the upper ocean of the offshore jet (Figs 8a and b). The angle $\phi_{Ri_g} = \tan^{-1}(-1/Ri_g)$, $Ri_g = N^2/\left(\mathrm{d}u_g/\mathrm{d}z\right)^2$, is another criterion for the frontal instability at submesoscale (Thomas et al., 2013). The estimates of ϕ_{Ri_g} in this front fall in between –90° and –45°, which is consistent with the pattern of negative Ertel PV in the elongated frontal zone (Fig. 8c), and also indicative of the favorable conditions for the SI. The cross-front vertical distribution of the Ertel PV and its decomposed terms show that a negative Ertel PV is injected into the oceanic interior along the outcropping isopycnals by the strong downwelling at the density front (Figs 8d and e). To quantify the possibility of SI, we also calculated the cumulative distribution function (CDF). The value of CDF is approximately 70% (Fig. 8f), which implies that SI is the most probable instability at this front case, similar to the fontal analysis results in the Antarctic Circumpolar Current (Barkan et al., 2015).

Although the PV tends to be conservative in the oceanic interior, it can be removed by atmospheric forcing and enhanced

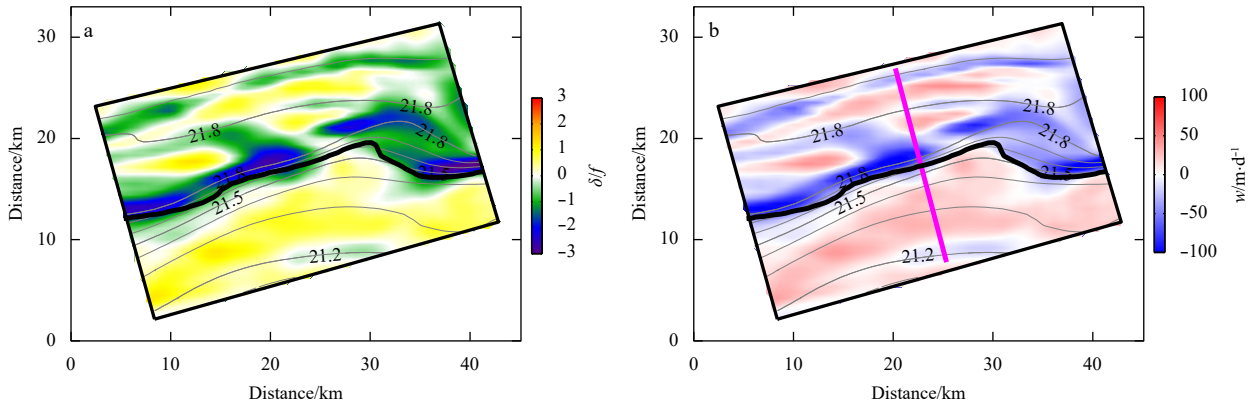

Fig. 6. Maps at 10 m of divergence normalized by f (shading) (a) and vertical velocity (shading) (b). The gray contours represent isopycnals with a spacing of 0.1 kg/m^3.

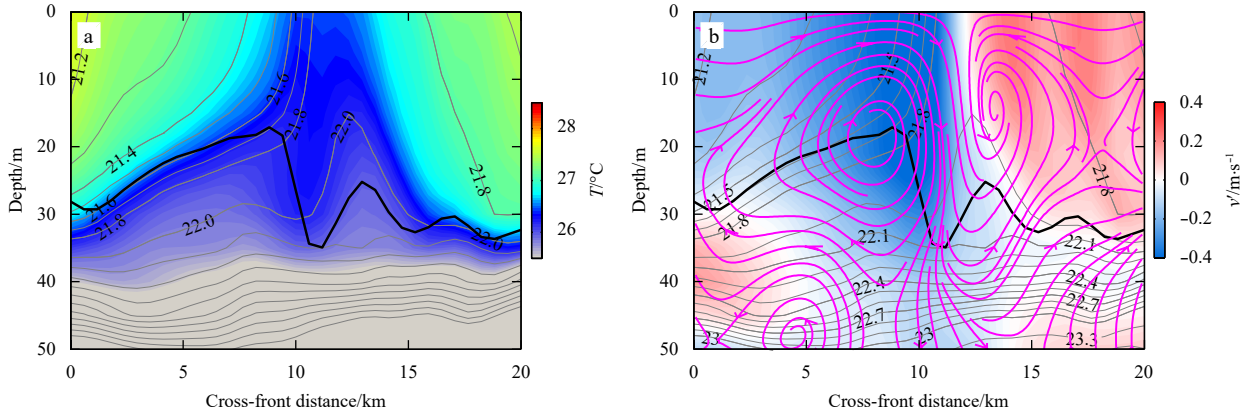

Fig. 7. Cross-front slices of temperature (shading) (a) and streamlines (vectors) (b) with along-front velocity anomaly (shading). The gray contours represent isopycnals with a spacing of 0.1 kg/m^3.

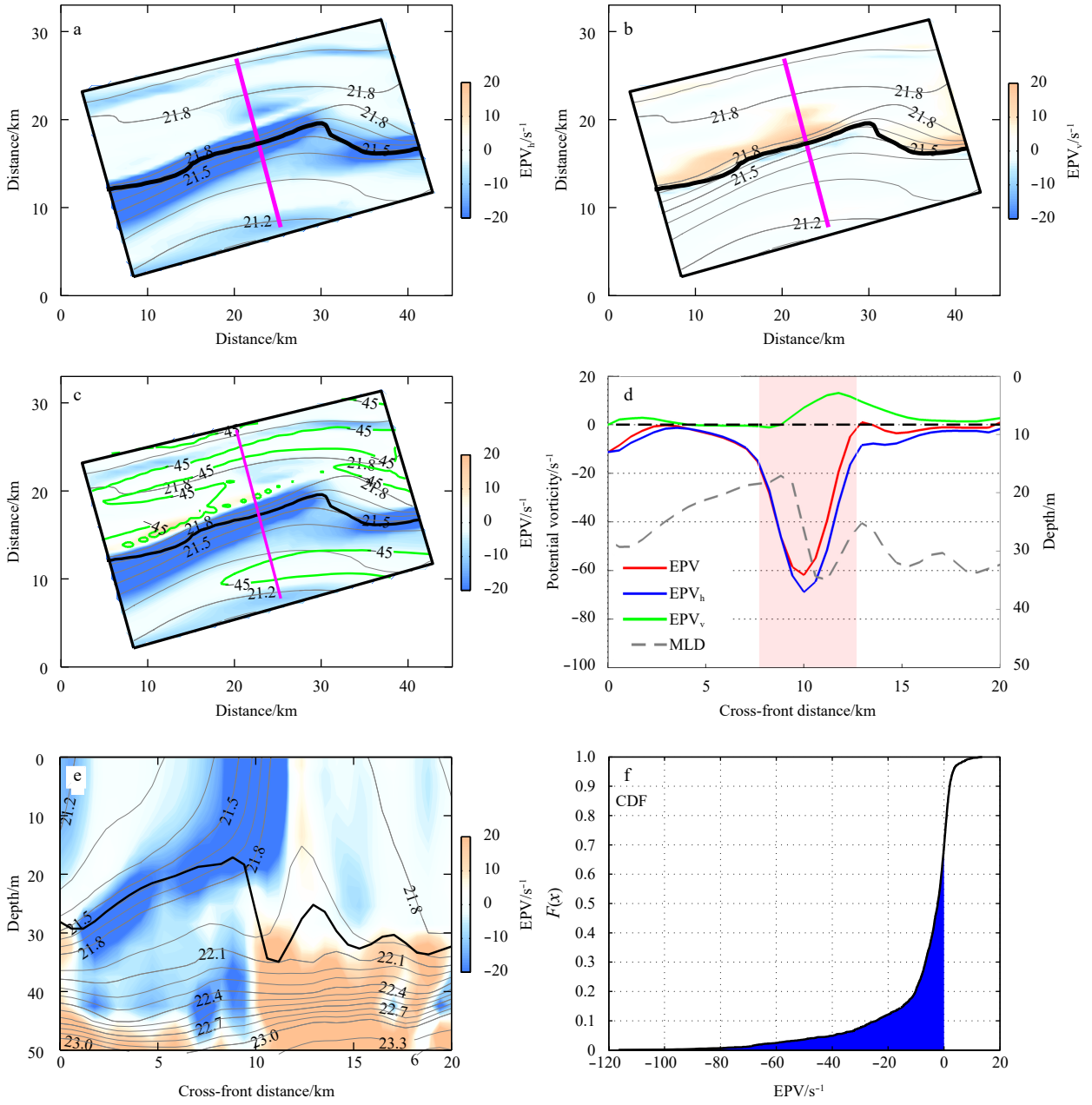

Fig. 8. Horizontal distribution of Ertel PV_h (a), Ertel PV_v (b), and Ertel PV (c) averaged over the MLD normalized by f^2 (shading), respectively; instantaneous cross-front profiles (magenta line in Fig. 8c) of Ertel PV_h, Ertel PV_v, and Ertel PV (d); vertical profiles of Ertel PV (shading) (e); and cumulative distribution function (CDF) of SI (the condition for SI is Ertel PV<0) (f). The gray contours in a–c and e represent isopycnals with a spacing of 0.1 kg/m^3. The green line in c denotes an angle of –45° for ϕ_{Ri_g}. The shaded region in d is the frontal zone and the gray dashed line denotes the MLD.

baroclinicity in density fronts (Thomas, 2005). As shown in Fig. 9, the wind direction is along the geostrophic current near the offshore jet, that is, the down-front wind has a significant impact on the frontal jet by driving a nonlinear Ekman transport and advecting cold water over warm water. The down-front wind forced Ekman transport can reduce the frontal stratification at the submesoscales (Thomas and Lee, 2005; D'Asaro et al., 2011). These conditions amplify the EBF to the order of $O(10^{-5})$ m^2/s^3 and increase the convective mixing of the buoyancy at the frontal jet. By this process, the destratification caused by the wind forcing contributes a negative PV injection and exacerbates the frontal instabilities.

As a result of the frontal submesoscale instabilities, the ageostrophic secondary circulations crossing the fronts develop, and provide a pathway for enhancing the vertical exchange of heat, momentum, and tracers between the surface and oceanic interior. Furthermore, the secondary circulation can effectively redistribute the buoyancy in the mixed layer and tend to restore the frontal flows to geostrophic balance (Boccaletti et al., 2007; Taylor and Ferrari, 2009; Gula et al., 2014). As the schematic in Fig. 10 shows, the submesoscale processes associated down-front wind forcing and frontal instabilities likely provide a new physical understanding for the enhanced nutrient supply for phytoplankton bloom at the fronts and filaments detected from satel-

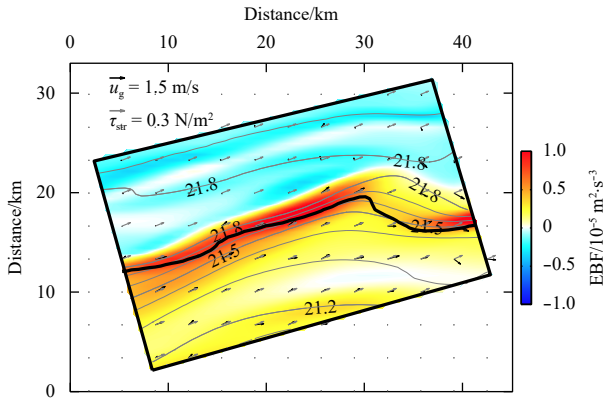

Fig. 9. Spatial distribution of EBF (shading) at the same time as Fig. 4b from ROMS2 in the frontal zone of the jet. The geostrophic velocity (wind stress) is shown in black (gray) arrows. The thin gray contours represent isopycnals with a spacing of 0.1 kg/m^3.

lite images in the WSCS (Fig. 3). This dynamical process can contribute the total tracers supply in the similar frontal zone according to the result of Omand et al. (2015).

4 Balanced geostrophic energy transition with frontal instability

Theoretical arguments show that submesoscale instabilities not only contribute to enhanced vertical exchanges, but also play an important role in the forward energy cascade of the geostrophic energy (Molemaker et al., 2010; Capet et al., 2008). At the submesoscale density front of the WSCS, the Ertel PV is negative and the ratio of the convective layer depth (h) to MLD (H) is $h/H \approx 0.3 < 1$. This result means that the wind-forced shear dominates over the convection (Thomas et al., 2013) and the shear production is the major contributor to the downscale geostrophic KE in this region (Thomas et al., 2016). With the weakening of the fronts by the ageostrophic secondary circulation, the submesoscale instabilities drive a destabilizing momentum flux to restore the geostrophic balance (Fig. 10). The geostrophic shear KE is drawn at the rate of GSP from larger-scale frontal flows (Thomas and Taylor, 2010). A subsequent slumping of the isopycnals arising from the geostrophic adjustment is expected to lead to a release of the APE stored in the fronts at the rate of BFLUX.

As shown in Fig. 11, both the energy conversion rates, namely GSP and BFLUX, which are the two primary energy sources for the submesoscale turbulence, are particularly large along the density front. The large positive GSP and BFLUX are mostly located in the frontal zone of the offshore jet with a magnitude of the order of $O(10^{-6})$ m^2/s^3, which is comparable to the scaling mixing caused by wind and surface buoyancy flux (Nagai et al., 2012), even though these parameters are decaying quickly out of the front. The large positive GSP and BFLUX are found in the frontal jet of the WSCS, indicating an effective forward energy cascade.

The vertical distributions of GSP and BFLUX are similar to those of the Ertel PV. The large values are primarily located in the central part of the frontal jet and they rapidly decrease away from the jet (Fig. 12). A negative $\overline{u'w'}$ is a result of the vertical exchange of momentum associated with the frontal instability and the ageostrophic secondary circulations owing to the strong negative vertical velocity. Therefore, the positive GSP arises in the upper ocean. The other important energy conversion term, BFLUX, is positive over much of the MLD, especially near the frontal jet, where it has a strong vertical velocity and abnormal buoyancy, which is consistent with the previous results (Thomas and Taylor, 2010). These diagnostic results suggest that the frontal submesoscale instabilities can effectively facilitate the energy conversion from the background geostrophic flows and feed the submesoscale turbulence in the upper ocean.

Additionally, the intensity of GSP is scaled with EBF; however, the contribution of BFLUX is only 1/3 of the GSP (Fig. 13a). These results agree with the conclusion that the EBF scales with the strength of GSP and BFLUX if the atmospheric forced surface buoyancy loss is not taken into account in a large eddy simula-

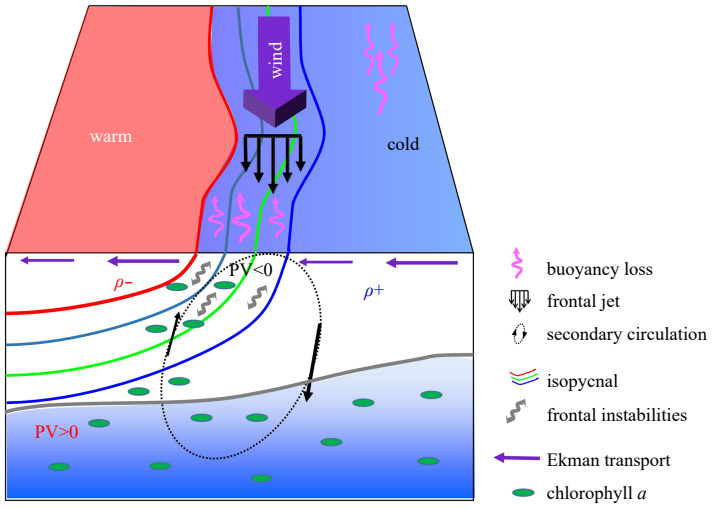

Fig. 10. Schematic diagram of the submesoscale front (similar with D'Asaro et al., 2011) associated with wind forcing and the cross-front ageostrophic secondary circulation. The Ekman transport cross-front transports cold water to the warm side of the front under the effect of down-front wind forcing, thus reducing the stratification and PV. The negative Ertel PV is conducive to submesoscale instability. The submesoscale instability effectively extracts energy from frontal jet and drives a cross-front ageostrophic secondary current to enhance vertical communication and restore geostrophic balance. $\rho^+(\rho^-)$ denotes the positive (negative) anomaly of density.

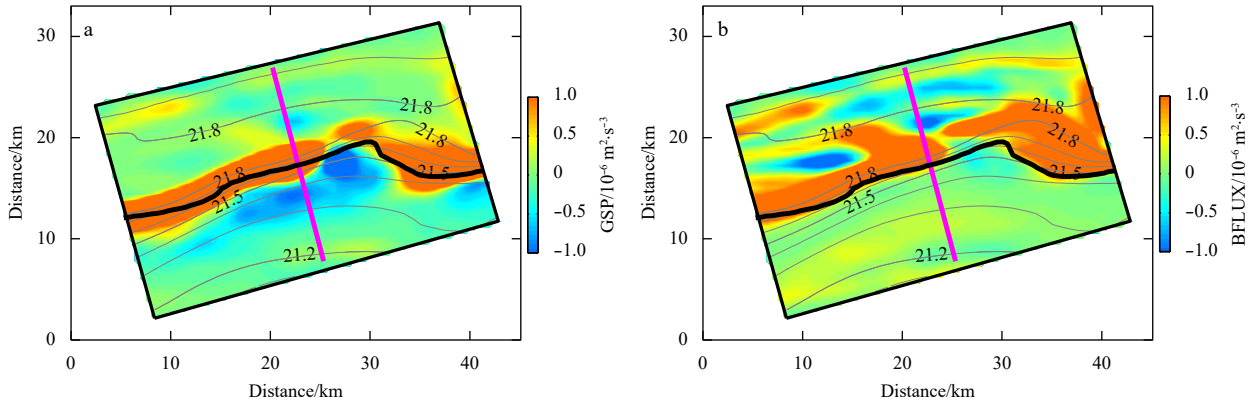

Fig. 11. Horizontal distribution of mean energy conversion terms in MLD (shading): GSP (a) and BFLUX (b). The gray contours represent isopycnals with a spacing of 0.1 kg/m³.

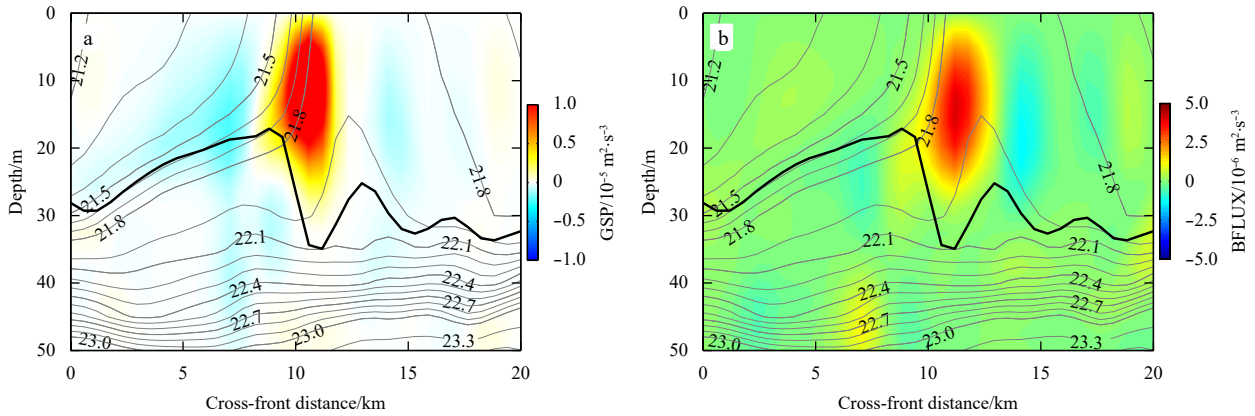

Fig. 12. Section of the energy conversion terms (shading): GSP (a) and BFLUX (b). The gray contours represent isopycnals with a spacing of 0.1 kg/m³.

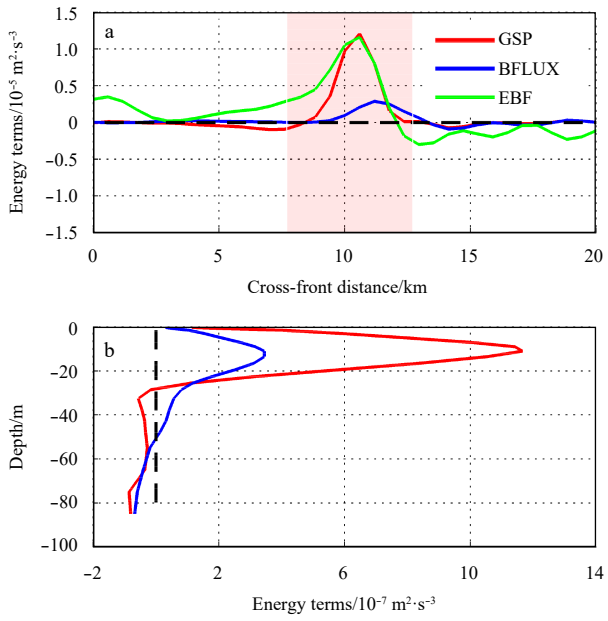

Fig. 13. Profiles of the instantaneous local energy conversion terms, GSP, BFLUX, and EBF averaged over the boundary layer (a); and the same quantities horizontally averaged on the section (b). The shading in a indicates the frontal zone. The black dashed line in a and b denotes a value of 0.

tion (LES) (Thomas, 2005; Thomas and Taylor, 2010). It suggests that the GSP is likely the dominant energy source for the submesoscale turbulent KE in the fronts of the WSCS. The submesoscale processes associated with the down-front wind forcing can partly contribute to the enhanced air-sea interactions in the WSCS (Xie et al., 2003). Moreover, as detected from the vertical profiles, the GSP and BFLUX quickly grow with depth in the Ekman layer (Fig. 13b). The maximum GSP appears at approximately 15 m, while the BFLUX reaches a maximum at approximately 18 m owing to the strong vertical velocity. Then, both the GSP and BFLUX rapidly reduce with depth. These results indicate that the submesoscale fronts and their instabilities can enhance the dissipation of geostrophic KE and transport energy towards a smaller scale but above the scale of Kolmogorov dissipation (Su et al., 2016).

5 Summary

The surface density fronts are ubiquitous in the SCS and their underlying dynamic effects at submesoscale are examined using a fine-resolution nested simulation in the frontal jet of the WSCS during the summer. Both the fine-resolution satellite images and the model results show active submesoscale fronts on the offshore jet system. Unlike in the geostrophic theory (Charney, 1971), here, these submesoscale fronts are characterized with unbalanced three-dimensional motions with a typical time scale of O(hour–day), a lateral scale of O(1–10) km, and an order of one of Ro and Ri.

The summer offshore jet with surface cooling is a common phenomenon in the WSCS owing to the southwest wind forcing. The high-resolution simulation and diagnostic results indicate that the cross-front Ekman transport, driven by the down-front wind forcing advects cold water to the warm water, effectively enhancing the vertical shear and reducing the frontal stratification. The enhanced vertical shear and the lateral buoyancy gradients intensify the frontal baroclinicity, thus contributing a negative Ertel PV in conjunction with the surface atmospheric forcing at approximately 5 km submesoscale front. More importantly, the conditions (e.g., negative Ertel PV, ϕ_{Ri_g} mostly varying within a range of –90° to –45°, and the CDF of SI being up to 70%) are conducive to the submesoscale SI. Owing to the frontal instabilities, the ageostrophic secondary circulation can develop, crossing the active submesoscale fronts. Such an ageostrophic process can redistribute the buoyancy for restoring the geostrophic balance by the submesoscale instabilities. Meanwhile, the submesoscale frontal vertical velocity is obviously increased to approximately 100 m/d, which is one order greater than that of the mesoscale. Enhanced vertical velocity contributes to the vertical exchanges and provides a new physical explanation for the frontal phytoplankton blooms in the WSCS.

The frontal instabilities at the submesoscale also provide an effective downscale energy pathway for the frontal geostrophic flows in the presence of a negative PV. The shear production caused by the ageostrophic secondary circulation can effectively extract the geostrophic KE at the rate of GSP, and the APE stored at the front is released at the rate of BFLUX. Both the diagnostic energy conversion rates, GSP and BFLUX, are particularly large in the frontal zone of the WSCS. The order of magnitude of GSP is scaled with EBF, while BFLUX contributes only 1/3 of the GSP, suggesting that the GSP in the density front of the WSCS plays a leading role in the mesoscale energy dissipation. Both the maxima of GSP and BFLUX are located in the submesoscale front, suggesting an effective downscale energy transfer. These results imply that down-front wind forced submesoscale processes likely provide downscale energy pathway in the WSCS from the larger-scale geostrophic flows to the submesoscale turbulence.

Acknowledgements

We thank GHRSST-PP (http://ghrsst-pp.metoffice.com), AVISO+ (http://www.aviso.altimetry.fr), NODC/NOAA (http://data.nodc.noaa.gov), and ESA (ftp://merisfrs-ftp-ds.eo.esa.int) for providing a suite of high-resolution satellite data and reanalysis products.

References

Barkan R, Winters K B, Smith S G L. 2015. Energy cascades and loss of balance in a reentrant channel forced by wind stress and buoyancy fluxes. Journal of Physical Oceanography, 45(1): 272–293, doi: 10.1175/JPO-D-14-0068.1

Boccaletti G, Ferrari R, Fox-Kemper B. 2007. Mixed layer instabilities and restratification. Journal of Physical Oceanography, 37(9): 2228–2250, doi: 10.1175/JPO3101.1

Capet X, McWilliams J C, Molemaker M J, et al. 2008. Mesoscale to submesoscale transition in the California current system. Part I: Flow structure, eddy flux, and observational tests. Journal of Physical Oceanography, 38(1): 29–43, doi: 10.1175/2007JPO3671.1

Carton J A, Giese B S. 2008. A reanalysis of ocean climate using Simple Ocean Data Assimilation (SODA). Monthly Weather Review, 136(8): 2999–3017, doi: 10.1175/2007MWR1978.1

Charney J G. 1971. Geostrophic turbulence. Journal of the Atmospheric Sciences, 28(6): 1087–1095, doi: 10.1175/1520-0469(1971)028<1087:GT>2.0.CO;2

Chen Gengxin, Gan Jianping, Xie Qiang, et al. 2012. Eddy heat and salt transports in the South China Sea and their seasonal modulations. Journal of Geophysical Research: Oceans, 117(C5): C05021

Chen Gengxin, Hou Yijun, Chu Xiaoqing. 2011. Mesoscale eddies in the South China Sea: Mean properties, spatiotemporal variability, and impact on thermohaline structure. Journal of Geophysical Research: Oceans, 116(C6): C06018

Chen Changlin, Wang Guihua. 2014. Interannual variability of the eastward current in the western South China Sea associated with the summer Asian monsoon. Journal of Geophysical Research: Oceans, 119(9): 5745–5754, doi: 10.1002/2014JC010309

Chu P C, Fan C W, Lozano C J, et al. 1998. An airborne expendable bathythermograph survey of the South China Sea, May 1995. Journal of Geophysical Research: Oceans, 103(C10): 21637–21652, doi: 10.1029/98JC02096

D'Asaro E, Lee C, Rainville L, et al. 2011. Enhanced turbulence and energy dissipation at ocean fronts. Science, 332(6027): 318–322, doi: 10.1126/science.1201515

Dong Jihai, Zhong Yisen. 2018. The spatiotemporal features of submesoscale processes in the northeastern South China Sea. Acta Oceanologica Sinica, 37(11): 8–18, doi: 10.1007/s13131-018-1277-2

Donlon C J, Martin M, Stark J, et al. 2012. The operational sea surface temperature and sea ice analysis (OSTIA) system. Remote Sensing of Environment, 116: 140–158, doi: 10.1016/j.rse.2010.10.017

Fang Wendong, Fang Guohong, Shi Ping, et al. 2002. Seasonal structures of upper layer circulation in the southern South China Sea from *in situ* observations. Journal of Geophysical Research: Oceans, 107(C11): 3202, doi: 10.1029/2002JC001343

Fox-Kemper B, Ferrari R, Hallberg R. 2008. Parameterization of mixed layer eddies. Part I: Theory and diagnosis. Journal of Physical Oceanography, 38(6): 1145–1165, doi: 10.1175/2007JPO3792.1

Gan Jianping, Li H, Curchitser E N, et al. 2006. Modeling South China sea circulation: Response to seasonal forcing regimes. Journal of Geophysical Research: Oceans, 111(C6): C06034

Gan Jianping, Qu Tangdong. 2008. Coastal jet separation and associated flow variability in the southwest South China Sea. Deep Sea Research Part I: Oceanographic Research Papers, 55(1): 1–19, doi: 10.1016/j.dsr.2007.09.008

Gula J, Molemaker M J, McWilliams J C. 2014. Submesoscale cold filaments in the gulf stream. Journal of Physical Oceanography, 44(10): 2617–2643, doi: 10.1175/JPO-D-14-0029.1

Gula J, Molemaker M J, McWilliams J C. 2015. Gulf stream dynamics along the southeastern U.S. seaboard. Journal of Physical Oceanography, 45(3): 690–715, doi: 10.1175/JPO-D-14-0154.1

Gula J, Molemaker M J, McWilliams J C. 2016. Submesoscale dynamics of a gulf stream frontal eddy in the south atlantic bight. Journal of Physical Oceanography, 46(1): 305–325, doi: 10.1175/JPO-D-14-0258.1

He Qingyou, Zhan Haigang, Cai Shuqun, et al. 2018. A new assessment of mesoscale eddies in the South China Sea: Surface features, three-dimensional structures, and thermohaline transports. Journal of Geophysical Research: Oceans, 123(7): 4906–4929, doi: 10.1029/2018JC014054

Hoskins B J. 1974. The role of potential vorticity in symmetric stability and instability. Quarterly Journal of the Royal Meteorological Society, 100(425): 480–482, doi: 10.1002/qj.49710042520

Hu Jianyu, Gan Jianping, Sun Zhenyu, et al. 2011. Observed three-dimensional structure of a cold eddy in the southwestern South China Sea. Journal of Geophysical Research: Oceans, 116(C5): C05016

Kuo N J, Zheng Quanan, Ho C R. 2000. Satellite observation of upwelling along the western coast of the South China Sea. Remote Sensing of Environment, 74(3): 463–470, doi: 10.1016/S0034-4257(00)00138-3

Large W G, McWilliams J C, Doney S C. 1994. Oceanic vertical mixing: a review and a model with a nonlocal boundary layer parameterization. Reviews of Geophysics, 32(4): 363–403, doi: 10.1029/

94RG01872
Lemarié F, Kurian J, Shchepetkin A F, et al. 2012. Are there inescapable issues prohibiting the use of terrain-following coordinates in climate models?. Ocean Modelling, 42: 57–79, doi: 10.1016/j.ocemod.2011.11.007
Li Yuanlong, Han Weiqing, Wilkin J L, et al. 2014. Interannual variability of the surface summertime eastward jet in the South China Sea. Journal of Geophysical Research: Oceans, 119(10): 7205–7228, doi: 10.1002/2014JC010206
Liu Xiao, Levine N M. 2016. Enhancement of phytoplankton chlorophyll by submesoscale frontal dynamics in the North Pacific Subtropical Gyre. Geophysical Research Letters, 43(4): 1651–1659, doi: 10.1002/2015GL066996
Liu Fenfen, Tang Shilin, Chen Chuqun. 2015. Satellite observations of the small-scale cyclonic eddies in the western South China Sea. Biogeosciences, 12(2): 299–305, doi: 10.5194/bg-12-299-2015
Mahadevan A, Tandon A. 2006. An analysis of mechanisms for submesoscale vertical motion at ocean fronts. Ocean Modelling, 14(3–4): 241–256, doi: 10.1016/j.ocemod.2006.05.006
McWilliams J C. 2016. Submesoscale currents in the ocean. Proceedings of the Royal Society A-Mathematical Physical and Engineering Sciences, 472(2189): 20160117, doi: 10.1098/rspa.2016.0117
McWilliams J C. 2017. Submesoscale surface fronts and filaments: secondary circulation, buoyancy flux, and frontogenesis. Journal of Fluid Mechanics, 823: 391–432, doi: 10.1017/jfm.2017.294
McWilliams J C. 2019. A survey of submesoscale currents. Geoscience Letters, 6: 3, doi: 10.1186/s40562-019-0133-3
McWilliams J C, Molemaker M J, Yavneh I. 2001. From stirring to mixing of momentum: Cascades from balanced flows to dissipation in the oceanic interior. In: Proceedings of the 12th 'Aha Huliko'a Hawaiian Winter Workshop. Hawaii: University of Hawaii, 59–66
Metzger E J. 2003. Upper ocean sensitivity to wind forcing in the South China Sea. Journal of Oceanography, 59(6): 783–798, doi: 10.1023/B:JOCE.0000009570.41358.c5
Nagai T, Tandon A, Yamazaki H, et al. 2012. Direct observations of microscale turbulence and thermohaline structure in the Kuroshio Front. Journal of Geophysical Research: Oceans, 117(C8): C08013
Omand M M, D'Asaro E A, Lee C M, et al. 2015. Eddy-driven subduction exports particulate organic carbon from the spring bloom. Science, 348(6231): 222–225, doi: 10.1126/science.1260062
Penven P, Debreu L, Marchesiello P, et al. 2006. Evaluation and application of the ROMS 1-way embedding procedure to the central california upwelling system. Ocean Modelling, 12(1–2): 157–187, doi: 10.1016/j.ocemod.2005.05.002
Risien C M, Chelton D B. 2008. A global climatology of surface wind and wind stress fields from eight years of QuikSCAT scatterometer data. Journal of Physical Oceanography, 38(11): 2379–2413, doi: 10.1175/2008JPO3881.1
Shchepetkin A F, McWilliams J C. 2005. The regional oceanic modeling system (ROMS): a split-explicit, free-surface, topography-following-coordinate oceanic model. Ocean Modelling, 9(4): 347–404, doi: 10.1016/j.ocemod.2004.08.002
Su Zhan, Ingersoll A P, Stewart A L, et al. 2016. Ocean convective available potential energy. Part I: Concept and calculation. Journal of Physical Oceanography, 46(4): 1081–1096, doi: 10.1175/JPO-D-14-0155.1
Su Zhan, Wang Jinbo, Klein P, et al. 2018. Ocean submesoscales as a key component of the global heat budget. Nature Communications, 9: 775, doi: 10.1038/s41467-018-02983-w
Taylor J R, Ferrari R. 2009. On the equilibration of a symmetrically unstable front via a secondary shear instability. Journal of Fluid Mechanics, 622: 103–113, doi: 10.1017/S0022112008005272
Thomas L N. 2005. Destruction of potential vorticity by winds. Journal of Physical Oceanography, 35(12): 2457–2466, doi: 10.1175/JPO2830.1
Thomas L N. 2012. On the effects of frontogenetic strain on symmetric instability and inertia-gravity waves. Journal of Fluid Mechanics, 711: 620–640, doi: 10.1017/jfm.2012.416
Thomas L N, Lee C M. 2005. Intensification of ocean fronts by down-front winds. Journal of Physical Oceanography, 35(6): 1086–1102, doi: 10.1175/JPO2737.1
Thomas L N, Tandon A, Mahadevan A. 2008. Submesoscale processes and dynamics. In: Hecht M W, Hecht H, eds. Ocean Modeling in an Eddying Regime. Washington DC: Geophysical Monograph Series, 17–38
Thomas L N, Taylor J R. 2010. Reduction of the usable wind-work on the general circulation by forced symmetric instability. Geophysical Research Letters, 37(18): L18606
Thomas L N, Taylor J R, D'Asaro E A, et al. 2016. Symmetric instability, inertial oscillations, and turbulence at the gulf stream front. Journal of Physical Oceanography, 46(1): 197–217, doi: 10.1175/JPO-D-15-0008.1
Thomas L N, Taylor J R, Ferrari R, et al. 2013. Symmetric instability in the Gulf Stream. Deep Sea Research Part Ⅱ: Topical Studies in Oceanography, 91: 96–110, doi: 10.1016/j.dsr2.2013.02.025
Wang Guihua, Chen Dake, Su Jilan. 2006. Generation and life cycle of the dipole in the South China Sea summer circulation. Journal of Geophysical Research: Oceans, 111(C6): C06002
Wang Guihua, Chen Dake, Su Jilan. 2008. Winter eddy genesis in the eastern South China Sea due to orographic wind jets. Journal of Physical Oceanography, 38(3): 726–732, doi: 10.1175/2007JPO3868.1
Wang Guihua, Su Jilan, Chu P C. 2003. Mesoscale eddies in the South China Sea observed with altimeter data. Geophysical Research Letters, 30(21): 2121, doi: 10.1029/2003GL018532
Wang Guihua, Wang Chunzai, Huang Ruixin. 2010. Interdecadal variability of the eastward current in the South China Sea associated with the summer Asian Monsoon. Journal of Climate, 23(22): 6115–6123, doi: 10.1175/2010JCLI3607.1
Woodruff S D, Worley S J, Lubker S J, et al. 2011. ICOADS Release 2.5: extensions and enhancements to the surface marine meteorological archive. International Journal of Climatology, 31(7): 951–967, doi: 10.1002/joc.2103
Wunsch C, Ferrari R. 2004. Vertical mixing, energy, and the general circulation of the oceans. Annual Review of Fluid Mechanics, 36: 281–314, doi: 10.1146/annurev.fluid.36.050802.122121
Wyrtki K. 1961. Physical oceanography of the southeast Asian waters. NAGA Report Vol. 2, Scientific Results of Marine Investigations of the South China Sea and the Gulf of Thailand. La Jolla, California: Scripps Institution of Oceanography, 195
Xie Shangping, Chang C H, Xie Qiang, et al. 2007. Intraseasonal variability in the summer South China Sea: Wind jet, cold filament, and recirculations. Journal of Geophysical Research: Oceans, 112(C10): C10008, doi: 10.1029/2007JC004238
Xie Shangping, Xie Qiang, Wang Dongxiao, et al. 2003. Summer upwelling in the South China Sea and its role in regional climate variations. Journal of Geophysical Research: Oceans, 108(C8): 3261, doi: 10.1029/2003JC001867
Xie Lingling, Zheng Quanan. 2017. New insight into the South China Sea: Rossby normal modes. Acta Oceanologica Sinica, 36(7): 1–3, doi: 10.1007/s13131-017-1077-0
Xie Lingling, Zheng Quanan, Zhang Shuwen, et al. 2018. The Rossby normal modes in the South China Sea deep basin evidenced by satellite altimetry. International Journal of Remote Sensing, 39(2): 399–417, doi: 10.1080/01431161.2017.1384591
Xiu Peng, Chai Fei. 2011. Modeled biogeochemical responses to mesoscale eddies in the South China Sea. Journal of Geophysical Research: Oceans, 116(C10): C10006, doi: 10.1029/2010JC006800
Yang Qingxuan, Nikurashin M, Sasaki H, et al. 2019. Dissipation of mesoscale eddies and its contribution to mixing in the northern South China Sea. Scientific Reports, 9: 556
Yu Jie, Zheng Quanan, Jing Zhiyou, et al. 2018. Satellite observations of sub-mesoscale vortex trains in the western boundary of the South China Sea. Journal of Marine Systems, 183: 56–62, doi: 10.1016/j.jmarsys.2018.03.010
Zhang Huaimin, Bates J J, Reynolds R W. 2006. Assessment of composite global sampling: Sea surface wind speed. Geophysical Research Letters, 33(17): L17714, doi: 10.1029/2006GL027086

Zhang Zhengguang, Qiu Bo, Klein P, et al. 2019. The influence of geostrophic strain on oceanic ageostrophic motion and surface chlorophyll. Nature Communications, 10: 2838, doi: 10.1038/s41467-019-10883-w

Zhang Zhiwei, Tian Jiwei, Qiu Bo, et al. 2016. Observed 3D structure, generation, and dissipation of oceanic mesoscale eddies in the South China Sea. Scientific Reports, 6: 24349, doi: 10.1038/srep24349

Zheng Quanan, Lin Hui, Meng Junmin, et al. 2008. Sub-mesoscale ocean vortex trains in the Luzon Strait. Journal of Geophysical Research: Oceans, 113(C4): C04032

Zheng Quanan, Xie Lingling, Xiong Xuejun, et al. 2020. Progress in research of submesoscale processes in the South China Sea. Acta Oceanologica Sinica, 39(1): 1–13, doi: 10.1007/s13131-019-1521-4

Zheng Quanan, Xie Lingling, Zheng Zhewen, et al. 2017. Progress in research of mesoscale eddies in the South China Sea. Advances in Marine Science (in Chinese), 35(2): 131–158